Supporting Information for

Characterization of the polarisation transfer to fluorinated pyridines in SABRE

J. Eronen, S. K.-M. Svensson, N. Hossain, V. V. Zhivonitko, J. Vaara, and A. M. Kantola

May 28, 2025

Contents

List of Figures

List of Tables

S1 Experimental details

Table S1: Parahydrogen source used in each experiment.

Experiment	Source (mFP)[a]	Source (dFP)[b]
Field dependence	Bruker	Bruker
Relaxation time	Home-made	Home-made
Build-up time	Bruker	Home-made
OPSYd	Bruker	-

[a] 3-fluoropyridine. [b] 3,5-difluoropyridine.

Table S2: Parameters for the pulse programs.

Parameter	Fluorine	Proton	OPSYd
B_1 (MHz)	41.185	43.773	43.773
Centre frequency (ppm)	-128	6	7.5
Pulse length (μs)	56.5	8.6	7.65
Receiver gain	28	1	10
Number of points	32768	32768	32768
Dwell time (μs)	50	50	50
Max. gradient (mT/m)	-	-	132
Gradient length (μs)	-	-	800
Ramp length (μs)	-	-	100
Ramp steps	-	-	10
Stabilization delay (μs)	-	-	1000

In the normal single-pulse sequence, the homonuclear two-spin order terms are not observable, as the $\pi/2$-pulse turns them into multiple quantum coherences. To detect the two-spin order terms, double-quantum filtered OPSY sequence, displayed in Fig. S1, was used.

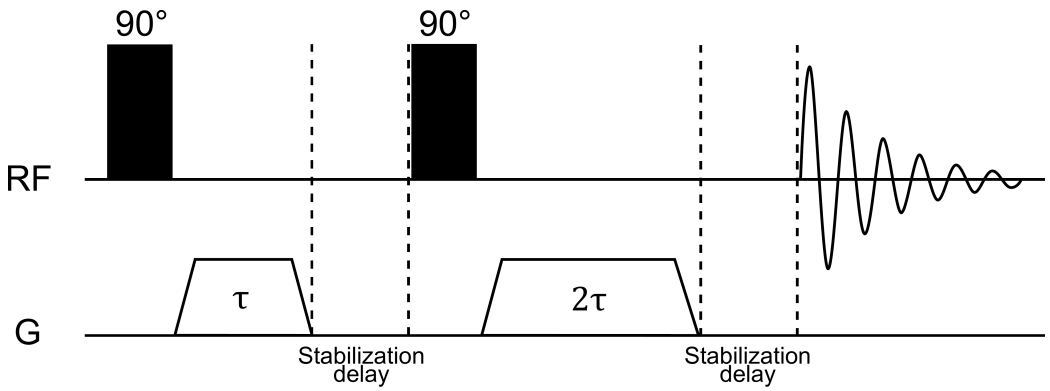

Figure S1: Double-quantum filtered OPSY sequence.

In order to avoid manually transferring the sample to another field for relaxation after it had been hyperpolarised, the sample was left in place and, instead, the magnetic field (magnetic flux density) was changed immediately after the parahydrogen flow was cut off. Due to excessive heating of the solenoids, the optimum polarisation transfer field could not be used in all the relaxation time experiments. However, the polarisation transfer fields were chosen such that sufficient in-phase magnetization was generated for the nucleus under study. The corresponding polarisation transfer field values for each relaxation field are shown in Table S3.

Table S3: Relaxation field values and their corresponding polarisation transfer fields.

Relaxation field	Polarisation field (^{19}F)	Polarisation field (^{1}H)
5 μT	5 μT	2 mT
50 μT	5 μT	2 mT
0.5 mT	5 μT	2 mT
8 mT	8 mT	8 mT
1 T	5 μT	8 mT

The NMR data was processed in the MestReNova V.14.0.1 software. First, the free induction decay was truncated (8192 pt) and apodized (1 Hz) to remove excessive noise and to improve SNR. Phase correction was applied using the thermally polarised spectrum as a reference. The baseline was corrected using a polynomial fit, and the peaks were manually integrated.

Since the resolution was insufficient for distinguishing the different ^{1}H peaks, integration was performed over all the ^{1}H peaks of the substrate. Further processing was carried out in Excel, where the polarisation levels were calculated, and in OriginPro 2022b, where the plots were generated and fitting of exponential functions was performed.

S2 Modelling details

This section contains further details about the spin dynamics simulations described in Section 3 of the main article. The code for an example computation can be found in the supplementary "SI_Code_example.m".

S2.1 Spin-operator basis set

Simulating the relatively large 14-spin systems was rendered possible by using a truncated operator basis set that was constructed by dropping the operators corresponding to five-spin order or above.[1,2] For example, a product operator $\hat{T}^{(1)}_{l_1 q_1} \otimes \hat{T}^{(2)}_{l_2 q_2} \otimes \hat{T}^{(3)}_{l_3 q_3} \otimes \hat{T}^{(4)}_{l_4 q_4} \otimes \hat{E}^{(5)} \otimes \cdots \otimes \hat{E}^{(14)}$, where, for K:th nucleus, $\hat{T}^{(K)}_{l_K q_K}$ is a one-spin irreducible spherical tensor operator of rank l_K and projection q_K and $\hat{E}^{(K)}$ is the one-spin unit operator, corresponds to four-spin order and is retained in the basis set. In contrast, a product operator $\hat{T}^{(1)}_{l_1 q_1} \otimes \hat{T}^{(2)}_{l_2 q_2} \otimes \hat{T}^{(3)}_{l_3 q_3} \otimes \hat{T}^{(4)}_{l_4 q_4} \otimes \hat{T}^{(5)}_{l_5 q_5} \otimes \cdots \otimes \hat{T}^{(14)}_{l_{14} q_{14}}$ corresponds to 14-spin order and is, therefore, dropped. This speeds up the simulations significantly, as otherwise the dimension of the untruncated Liouville space would scale as 4^n with the number of spins n. In the Spinach software, this basis set approximation is denoted "IK-0", and that label will be used when referring to the computational results. The quality of the results obtained with the simplified basis set could be tested for the 8-spin system, which was simulated both using the simplified basis set and the full basis set. The 7-spin system was only simulated using the full basis set.

S2.2 Interactions

Both coherent and incoherent interactions were taken into account in the simulations. The coherent interactions were the isotropic chemical shift and J-coupling. In the calculations featuring the incoherent mechanisms, the

relaxation superoperator was calculated using Bloch-Redfield-Wangsness relaxation theory,[3,4] assuming isotropic rotational diffusion as the underlying dynamical model. The implementation of this in the Spinach software is treated in Ref.[5] The incoherent interactions accounted for were the direct dipole-dipole coupling between all the nuclei and ^{14}N quadrupole coupling, including scalar relaxation of the second kind (SRSK). The SRSK contribution to the relaxation superoperator was calculated empirically according to the method of Abragam,[6] with the quadrupolar ^{14}N centres defined as sources of rapid relaxation. For comparison, there were also computations that omitted the SRSK mechanism. The nuclear coordinates, chemical shifts, J-couplings, and quadrupole couplings were adopted from density-functional theory (DFT) calculations described in Section S2.5 (*vide infra*).

The rotational correlation time was set to 30 ps. This was the choice of correlation time that, in Spinach simulations of inversion-recovery experiments, most closely reproduced the $T_1 = 0.91$ s relaxation time observed experimentally for ^{19}F nuclei in the axial mFP-ligand of the SABRE-complex, at 14.1 T. These inversion-recovery simulations included, in addition to all other mechanisms mentioned, the ^{19}F chemical shift anisotropy (CSA) contribution in the relaxation, since CSA is important at such high magnetic fields for a fluorine centre.

The relaxation superoperator was thermalised using the Levitt-Di Bari method[7] at the temperature of 298 K. The simulations that included relaxation and the SRSK mechanism for the 14-spin systems at μT-magnetic fields were run without thermalisation, due to software limitations. At such a fairly high temperature, for such low magnetic fields, this omission is not significant.

The imaginary parts of the relaxation superoperator, related to dynamic frequency shifts, were retained in the simulations.

S2.3 Chemical exchange

In a SABRE complex, both the hydride protons and the ligands to be hyperpolarised undergo chemical exchange with the corresponding free species, H_2 and the free fluoropyridine, respectively, in the solution. This gives each mFP or dFP molecule a finite polarisation time in the SABRE complex. This exchange process was modelled in the simulations by using a single-exponential weighting function with a decay corresponding to the ligand dissociation rate.[8] This very simplistic model of reaction kinetics has some merit to it,

since a computational study[9] has found that, for the corresponding SABRE-complex with non-fluorinated pyridine, the most likely exchange-reaction was one where both hydride and pyridine were exchanged simultaneously.

The ligand dissociation rate was set to $k_d = 19.6\ \mathrm{s}^{-1}$. This is the value found from the fit to a presently performed experiment in Table S12 (*vide infra*). In the simulations, the ligand dissociation rate was corrected to account for the size of the time step, Δt, according to[10]

$$k_{\mathrm{corrected}} = k_d \exp\left(-\frac{k_d \Delta t}{2}\right). \tag{S1}$$

S2.4 Numerical parameters

The various numerical parameters of the Spinach software were set somewhat stricter ($\times 10^{-2}$) than their default values, and, for the zero-track elimination, a maximum of 64 steps and a tolerance of 10^{-30} was set. For the 7-spin system, simulations were run with the very strict numerical settings that within the Spinach software are denoted "paranoid numerical accuracy settings". A total simulation length of 5 s was used and this duration was divided into either 10 000 or 100 000 time steps, Δt. The simulations of the 14-spin and 12-spin models of mFP, the simulations of the 8-spin system using a full operator basis set, the simulations of the 2-ligand/8-spin system, the simulations of the 6-spin system, and the simulation of dFP that included relaxation, all used 10 000 time steps. All the other simulations used 100 000 time steps.

A simulation time of 5 s was considered sufficient since the polarisation build-up time in the simulations is significantly shorter than in experiments. One of the major reasons for this is the simplified model for chemical exchange, which was exponential weighting of density modelling ligand-only exchange. We will in the future incorporate a more complete chemical exchange model including the hydride exchange, in simulations corresponding to the presently performed ones.

S2.5 Quantum-chemical data

The spin Hamiltonian parameters used in the spin dynamics simulations were obtained by using quantum-chemical calculations of the SABRE complexes with mFP and dFP ligands in the framework of density-functional theory (DFT). First, the complexes with both mFP and dFP were built and

geometry-optimized *in vacuo* on the Turbomole software[11] using the hybrid PBE0 exchange-correlation functional[12] supplemented with the DFT D3(BJ) dispersion correction.[13,14] The energy-consistent, quasirelativistic Stuttgart-Cologne pseudopotential with 60 electrons in the core, ECP60MDF,[15] and the corresponding def2-QZVPP valence basis set[16,17] were employed for the Ir centre, whereas the all-electron def2-QZVPP basis set[17] was used for the other atoms.

Whereas in the case of the symmetric dFP ligands, only one optimized geometry was sought, the complex with unsymmetric mFP ligands can take no less than altogether six distinct conformers. The relative statistical importance of the latter may be roughly assessed from the Boltzmann factors appropriate to the final total energy of the optimized complexes. In this consideration, a single conformer, denoted by us as "in-out-towards" (iot), turned out to have 73% occupation probability at 298 K temperature. This designation is based on the relative position of the fluorine substitution sites in the equatorial and axial ligands, with the fluorine site of the first equatorial ligand pointing "in" and that of the other pointing "out", when viewing towards the complex from the direction of these ligands, and the fluorine site of the axial ligand pointing "towards" the viewer, see Fig. S2. In the statistical weight of this conformer, we have taken into account the fact that it actually represents two equivalent conformers, iot and oit. The other conformers, iit, oot, ioa (the "a" representing the situation where the fluorine site of the axial ligand points "away" from the above-mentioned point-of-view), iia and ooa are higher up in energy, as evidenced by Table S4. The optimized structures of the iot conformer with mFP and the single conformation with dFP ligands are given in Tables S5 and S6, respectively. Corresponding .xyz files are found in a separate file named "xyz_files.zip". The further quantum-chemical and spin dynamics calculations used these two geometries.

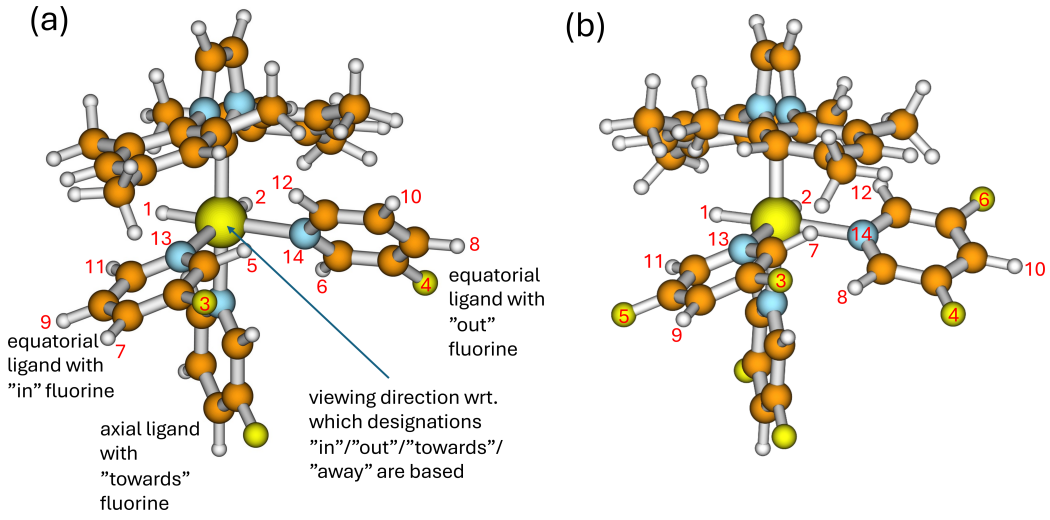

Figure S2: Optimized geometry of the SABRE complex with (a) mFP ligands in the iot ("in-out-towards") conformer and (b) dFP ligands. Ir atom in yellow (large sphere), carbons in orange, nitrogens in blue, fluorines in yellow (small spheres) and hydrogens in white. The numbering of the nuclei included in the spin dynamics model is indicated.

Table S4: Relative energies and statistical weights (at 298 K) of the optimized total energies of the six conformers of the SABRE complex with mFP ligands.

Conformer	Relative energy/kT	Statistical weight
iot	0.00	0.73
iit	4.30	0.00
ioa	4.15	0.01
iia	4.04	0.01
ooa	1.35	0.10
oot	0.92	0.15

Table S5: Optimized geometry of the iot conformer of the SABRE complex with mFP ligands. The .xyz format is used.

Atom	x (Å)	y (Å)	z (Å)	Atom	x (Å)	y (Å)	z (Å)
83							
H	0.1398240	1.6439053	-1.3060737	H	-2.3503887	-2.1154470	3.2130318
H	1.8274179	0.4353038	-0.6527717	H	-2.2556967	-0.7428845	4.2974681
F	-4.5494695	-2.4608498	-1.0762939	H	-0.9622054	-1.0140292	3.1478328
F	3.3929648	-4.1979363	-0.6198634	H	-3.0591589	3.4960263	-0.3522227
H	-2.2138624	-1.8675030	-0.2265224	H	-1.4706228	2.7065760	-0.3502276
H	2.4411780	-1.9091981	-1.3226375	H	-1.9915765	3.6330931	1.0449073
H	-5.3610375	-0.7518480	-2.8760610	H	-6.8602906	0.8458696	0.5089305
H	1.8928928	-5.3271308	1.1896737	H	-6.8575643	-0.2830902	1.8666012
H	-3.9361017	1.2008714	-3.5904467	H	-6.4243416	-0.8456278	0.2620826
H	-0.1943524	-4.2212801	2.0681563	H	2.7424576	-0.5464584	3.6354080
H	-1.7070923	1.4960972	-2.5527510	H	3.5631694	-1.7273855	2.6209396
H	-0.8211581	-1.9967074	1.1897339	H	1.9163903	-1.2100624	2.2385335
N	-1.8489176	-0.1574955	-1.3461032	H	2.8845180	4.2759693	-0.2998329
N	0.7487676	-1.8700346	-0.1273093	H	1.8453082	3.9927857	1.0979370
F	-0.1853596	-3.0971259	-5.0174877	H	1.4974587	3.1810627	-0.4213367
H	-0.5410912	-2.1506561	-2.6544378	H	6.9128605	1.6965913	-0.7765259
H	1.4147742	-1.5744520	-6.4094564	H	7.1292688	0.1785605	0.1034344
H	2.4252486	0.5235684	-5.4495535	H	7.3778688	1.7171460	0.9184448
H	1.8808881	1.1551602	-3.1104478	H	-1.1234623	2.0347386	3.8286344
N	0.6530263	-0.4568307	-2.7830251	H	1.6307329	2.2719611	3.6756012
C	-2.0411750	-1.0716914	3.2779071	H	-4.5991244	-1.3419302	2.5316510
C	-2.3390631	2.9569467	0.2605301	H	-4.8888395	2.0961553	0.0233219
C	-6.3376915	-0.0013293	0.9506083	H	5.3927661	-0.6352163	1.6320720
C	2.8865521	-0.8747430	2.6033450	H	4.9195887	3.1182568	-0.3431871
C	2.3068326	3.5203181	0.2289749	C	0.2125702	0.9009572	1.0519298
C	6.7587368	1.2001966	0.1813363	Ir	0.3003138	0.1557419	-0.7970376
N	-0.8376646	1.1590025	1.8857508	C	0.1144146	-1.5704177	-3.2881724
C	-0.4248888	1.7530261	3.0618526	C	0.3794944	-1.9798197	-4.5792118
N	1.2882302	1.3469729	1.7681880	C	1.2118902	-1.2484806	-5.3984518
C	0.9113573	1.8679357	2.9864382	C	1.7629028	-0.0966450	-4.8621785
C	-2.2118696	0.8636122	1.6474582	C	1.4673761	0.2675845	-3.5637305
C	-2.7930850	-0.2273369	2.2923923	C	0.0460613	-2.5134800	0.8095893
C	-2.9578542	1.7306923	0.8500614	C	0.4116723	-3.7497164	1.3071262
C	-4.1362047	-0.4890366	2.0477172	C	1.5569528	-4.3635011	0.8317022
C	-4.2969875	1.4328340	0.6435563	C	2.2753227	-3.6819288	-0.1285822
C	-4.9008896	0.3202339	1.2179800	C	1.8589146	-2.4496801	-0.5903066
C	2.6593271	1.3076046	1.3659732	C	-2.6011783	-1.1897948	-0.9710549
C	3.4439608	0.2271611	1.7580734	C	-3.8545513	-1.4121839	-1.5046614
C	3.1733736	2.3692018	0.6250867	C	-4.3792637	-0.5711850	-2.4599726
C	4.7702790	0.2055874	1.3470598	C	-3.5899826	0.4982293	-2.8452829
C	4.5055596	2.3053626	0.2427296	C	-2.3456670	0.6719000	-2.2719892
C	5.3182651	1.2313498	0.5874445				

Table S6: Optimized geometry of the SABRE complex with dFP ligands. The .xyz format is used.

Atom	x (Å)	y (Å)	z (Å)	Atom	x (Å)	y (Å)	z (Å)
83							
H	1.0109020	1.1825893	-1.1742763	H	-1.7819074	-1.7257133	4.1292857
H	1.9453830	-0.4853060	-0.1349946	H	-0.4944118	-1.4242503	2.9703038
F	-4.8750589	-0.6671912	-1.7275414	H	-1.6428767	-2.7433040	2.7074337
F	-2.0703297	-5.0388778	-0.5118855	H	-3.2990619	3.2238344	0.3147038
F	-2.3894726	2.2546955	-4.3906153	H	-1.6682405	2.5788077	0.0765674
F	1.6452617	-4.5406083	2.2763245	H	-2.1066918	3.3005396	1.6113205
H	-2.6842752	-0.8998587	-0.3955105	H	-6.7967515	0.0494329	2.0481952
H	-1.6348958	-2.5868271	-1.0896422	H	-6.3524720	-1.6496783	1.8826035
H	-4.5948181	0.9947966	-3.7349859	H	-6.4885088	-0.6220472	0.4543454
H	-0.3128792	-5.9350072	1.2257358	H	4.2924336	-0.2837440	3.1318123
H	-0.4486039	1.6218150	-2.8031858	H	3.7744699	-1.2320292	1.7511735
H	1.6621471	-2.1239823	1.3714452	H	2.5763361	-0.4088028	2.7598741
N	-1.4597759	0.3129571	-1.5565694	H	1.9048677	4.6007655	-0.5356574
N	0.0248336	-2.2311518	0.1110549	H	1.1888085	4.1632346	1.0158725
F	4.0236670	-1.4685369	-4.3390844	H	0.7995348	3.2257481	-0.4173249
F	-0.3498434	-2.8416720	-5.2393939	H	6.8931785	3.4777252	-0.0130560
H	2.2066998	-2.6440583	-5.8173404	H	6.3677382	2.8844500	-1.5803058
H	-0.8838090	-1.7165406	-2.9997631	H	7.1379261	1.7843951	-0.4320756
H	2.9895800	-0.4961441	-2.1763282	H	-1.0026907	1.7948228	3.9356125
N	1.0216890	-1.0702585	-2.4767953	H	1.6332811	2.5464973	3.5351621
C	-1.5354268	-1.7191391	3.0655018	H	-4.1323830	-2.1070279	2.5446125
C	-2.4843831	2.6839249	0.7931632	H	-4.9865877	1.6701760	0.7536035
C	-6.1657105	-0.6492143	1.4960919	H	5.7754606	0.5461680	1.0865947
C	3.5668350	-0.3215328	2.3180223	H	4.1357317	3.9972779	-0.8122272
C	1.6042591	3.7621742	0.0891975	C	0.3237781	0.7513968	1.1226235
C	6.4479154	2.6216954	-0.5248261	Ir	0.4878015	-0.1908532	-0.6218482
N	-0.6959807	0.8665427	2.0200173	C	0.1552569	-1.6815970	-3.2879763
C	-0.3214720	1.6054243	3.1258899	C	0.5592429	-2.2487967	-4.4806277
N	1.3379451	1.4497319	1.7131184	C	1.8749404	-2.2054155	-4.8866443
C	0.9566145	1.9705994	2.9299024	C	2.7417195	-1.5602704	-4.0274759
C	-2.0461864	0.4399819	1.8488204	C	2.3076219	-1.0035853	-2.8410823
C	-2.4570325	-0.7963202	2.3328445	C	-0.9439643	-3.0064479	-0.3752653
C	-2.9476794	1.3486866	1.2833368	C	-1.0835913	-4.3261464	0.0099606
C	-3.7993906	-1.1414622	2.1807131	C	-0.2206673	-4.9033158	0.9161083
C	-4.2769927	0.9736116	1.1857936	C	0.7710711	-4.0745663	1.3987425
C	-4.7230778	-0.2734087	1.6200423	C	0.8781284	-2.7596735	0.9910437
C	2.6242104	1.7181055	1.1505190	C	-2.6251827	-0.2685144	-1.2704042
C	3.6956762	0.8836600	1.4391783	C	-3.7485850	-0.0462109	-2.0453856
C	2.7649286	2.8561386	0.3529885	C	-3.7211163	0.8064677	-3.1267077
C	4.9299324	1.1909756	0.8735570	C	-2.5059149	1.4112423	-3.3776316
C	4.0117869	3.1196196	-0.1877375	C	-1.3986939	1.1527521	-2.5952677
C	5.1077994	2.2956290	0.0566258				

NMR shielding tensors were calculated at the optimized geometries, the above-mentioned basis sets, pseudopotential, exchange-correlation functional, and the gauge-including atomic orbital (GIAO) ansatz on the Turbomole code. The resulting shielding constants are listed in Table S7. Due to the use of the pseudopotential, the dominant scalar relativistic effects arising from the heavy Ir atom are included in the calculated shieldings, whereas the spin-orbit effects are neglected in the present calculations. The calculated ^{1}H shielding constants of the free mFP ligand (results not shown) and the hydride nuclei in the SABRE complex revealed a roughly 15-ppm upfield shift of the latter in computations, whereas experimentally no less than twice as large an upfield shift was observed presently. Protons directly bound to a heavy atom are susceptible to very strong spin-orbit coupling effects[18,19] and we de-

cided to correct their omission by empirically shifting the calculated hydride proton shielding constants by +15 ppm, to obtain the chemical shifts used in the spin dynamics simulations. The shift reference of $\sigma_{\mathrm{ref}} = 31.8$ ppm appropriate to tetramethylsilane was used for ^{1}H. The shift reference of 0 ppm was arbitrarily employed for both ^{19}F and ^{14}N nuclei. This is of no consequence as no spectra were calculated. The high-field simulations of the inversion-recovery experiment (to obtain the rotational correlation time) included the chemical shift anisotropy (CSA) relaxation mechanism (along with its small cross terms with the dipole-dipole mechanism). Hence, the appropriate, calculated full shielding tensors, expressed in the molecular frames given in Tables S5 and S6, are included in Table S8.

Table S7: Calculated nuclear shielding constants σ for the hydride protons and the NMR-active nuclei in the equatorial mFP (iot conformer, see the text) and dFP ligands.

	mFP complex			dFP complex		
Number	Element	Identity	σ (ppm)	Element	Identity	σ (ppm)
1	H	hydride	38.76[a]	H	hydride	38.87[a]
2	H	hydride	38.39[a]	H	hydride	39.08[a]
3	F	eq-ligand1 F	299.18	F	eq-ligand1 F "in"	290.66
4	F	eq-ligand2 F	295.30	F	eq-ligand2 F "in"	295.03
5	H	eq-ligand1 2-H	23.52	F	eq-ligand1 F "out"	293.05
6	H	eq-ligand2 2-H	23.92	F	eq-ligand2 F "out"	293.99
7	H	eq-ligand1 4-H	23.96	H	eq-ligand1 4-H	25.07
8	H	eq-ligand2 4-H	23.74	H	eq-ligand2 4-H	23.34
9	H	eq-ligand1 5-H	24.26	H	eq-ligand1 5-H	24.07
10	H	eq-ligand2 5-H	23.73	H	eq-ligand2 5-H	24.07
11	H	eq-ligand1 6-H	22.79	H	eq-ligand1 6-H	22.95
12	H	eq-ligand2 6-H	22.62	H	eq-ligand2 6-H	22.30
13	N	eq-ligand1 ^{14}N	-50.40	N	eq-ligand1 ^{14}N	-50.49
14	N	eq-ligand2 ^{14}N	-46.65	N	eq-ligand2 ^{14}N	-48.66

[a] Values subjected to an additional, empirical +15 ppm correction in the present spin dynamics calculations. The values indicated in the table are prior to the correction.

Table S8: Calculated ^{19}F and ^{14}N nuclear shielding tensors $\boldsymbol{\sigma}$ of the SABRE complexes with the mFP (iot conformer) and dFP ligands.

Atom number	Element	Identity	$\boldsymbol{\sigma}$ (ppm)		
Complex with mFP ligands					
3	F	eq-ligand1 F	262.43	-19.75	-50.78
			-10.68	317.21	43.52
			-59.04	39.52	317.90
4	F	eq-ligand2 F	307.94	19.77	41.73
			31.37	259.47	54.58
			30.39	62.37	318.51
13	N	eq-ligand1 ^{14}N	-96.99	-105.30	-118.64
			-111.01	-97.16	230.57
			-125.45	223.11	42.96
14	N	eq-ligand2 ^{14}N	-97.65	94.45	217.24
			108.22	-79.96	141.22
			200.79	132.57	37.65
Complex with dFP ligands					
3	F	eq-ligand1 F "in"	255.74	-13.88	-33.87
			-2.37	325.07	69.08
			-47.11	59.50	291.17
4	F	eq-ligand2F "in"	314.76	-1.63	-54.91
			-17.00	243.58	39.33
			-47.96	52.68	326.74
5	F	eq-ligand1 F "out"	232.28	-14.25	-44.58
			-23.97	339.13	46.16
			-26.35	50.46	307.74
6	F	eq-ligand2 F "out"	312.19	-42.41	-42.21
			-27.12	233.80	33.84
			-47.83	24.64	335.98
13	N	eq-ligand1 ^{14}N	-162.96	-105.34	-27.04
			-127.61	44.75	242.07
			-37.52	242.84	-33.25
14	N	eq-ligand2 ^{14}N	-70.40	-86.08	-248.02
			-76.89	-122.77	92.34
			-249.17	95.07	47.21

For the quadrupolar ^{14}N isotope, the interaction between the electric-field gradient (EFG) at the nuclear site and the nuclear electric quadrupole moment provides the main incoherent interaction, on account of the molec-

ular rotation. This mechanism also underlies the scalar relaxation of the second kind as considered in the present spin dynamics simulations. The above-mentioned quantum-chemical methodology was applied for obtaining the quadrupole coupling tensors $\boldsymbol{Q}$ appearing in the NMR spin Hamiltonian term of the form $\boldsymbol{I} \cdot \boldsymbol{Q} \cdot \boldsymbol{I}$, where $\boldsymbol{I}$ is the spin of the ^{14}N centre. This Hamiltonian, along with its small cross-terms with the dipole-dipole and CSA Hamiltonians, were included in the present spin dynamics simulations. The calculated EFG and $\boldsymbol{Q}$ tensors are listed in Table S9.

Table S9: Calculated ^{14}N electric-field gradient (EFG) and quadrupole coupling tensors $\boldsymbol{Q}$ of the SABRE complexes with the mFP (iot conformer) and dFP ligands.

Atom number	Identity	EFG (atomic units)			$\boldsymbol{Q}$ (MHz)		
Complex with mFP ligands							
13	eq-ligand1 ^{14}N	-0.490	-0.164	-0.416	-1.178	-0.393	-0.999
		-0.164	0.293	0.058	-0.393	0.703	0.140
		-0.416	0.058	0.198	-0.999	0.140	0.475
14	eq-ligand2 ^{14}N	0.215	0.288	0.005	0.516	0.692	0.012
		0.288	-0.437	0.375	0.692	-1.048	0.901
		0.005	0.375	0.222	0.012	0.901	0.533
Complex with dFP ligands							
13	eq-ligand1 ^{14}N	-0.372	0.088	-0.456	-0.893	0.212	-1.096
		0.088	0.359	0.206	0.212	0.863	0.495
		-0.456	0.206	0.013	-1.096	0.495	0.030
14	eq-ligand2 ^{14}N	0.313	-0.112	-0.103	0.752	-0.268	-0.246
		-0.112	-0.609	0.309	-0.268	-1.462	0.742
		-0.103	0.309	0.296	-0.246	0.742	0.710

Finally, the spin-spin coupling constants were calculated for the SABRE complex with mFP (iot conformer) and dFP ligands using the above-mentioned quantum-chemical methodology, retaining all the four contributions (Fermi contact, spin-dipolar, as well as orbital para- and diamagnetic terms). Spin-spin coupling constants to ^{19}F have traditionally been difficult for DFT-based methodology, such as the one employed here, particularly due to the Fermi contact term, and particularly for one-bond couplings between ^{19}F and other nuclei. Comparison calculations performed on the free mFP ligand could be carried out between the present method and the *ab initio* coupled-cluster singles and doubles (CCSD) method, the latter employed in the CFOUR code.[20]

This comparison (results not shown) indicates a very nice qualitative agreement of the presently relevant HH, NH, FH and NF coupling constants, none of which represents the one-bond coupling case, between the two methods. Hence, we assume that the PBE0-based coupling matrices obtained presently for the entire SABRE complexes are usable in the spin dynamics simulations. Tables S10 and S11 indicate the calculated total coupling constants for the complexes with mFP and dFP ligands, respectively.

Table S10: Calculated spin-spin coupling constants (in Hz) of the relevant nuclei in the SABRE complex with the mFP (iot conformer) ligands. Couplings for the isotopes ^{1}H, ^{14}N and ^{19}F are given.

		H 1	H 2	F 3	F 4	H 5	H 6	H 7	H 8	H 9	H 10	H 11	H 12	N 13
H	1													
H	2	-7.67												
F	3	-0.05	2.08											
F	4	1.87	-0.02	-0.07										
H	5	-0.03	1.77	1.34	-0.21									
H	6	1.65	0.39	-0.07	1.56	0.01								
H	7	0.02	0.01	5.69	-0.05	2.32	-0.05							
H	8	0.02	-0.02	-0.04	5.34	-0.03	2.38	-0.04						
H	9	-0.02	0.45	5.07	-0.06	0.62	-0.04	8.76	-0.05					
H	10	0.41	-0.10	0.00	4.80	0.11	0.63	-0.04	8.77	-0.05				
H	11	-0.10	1.49	-0.12	-0.07	-0.31	0.02	0.70	-0.06	5.80	-0.06			
H	12	1.42	0.08	-0.05	-0.23	-0.11	-0.31	-0.02	0.68	-0.05	5.66	-0.02		
N	13	-0.23	16.49	-3.56	-0.02	4.42	0.00	-0.32	0.00	2.11	0.00	4.76	-0.09	
N	14	15.32	-0.41	0.00	-2.85	0.07	3.77	0.00	-0.32	0.00	2.13	-0.03	4.96	0.00

Table S11: Calculated spin-spin coupling constants (in Hz) of the relevant nuclei in the SABRE complex with the dFP ligands. Couplings for the isotopes ^{1}H, ^{14}N and ^{19}F are given.

		H 1	H 2	F 3	F 4	F 5	F 6	H 7	H 8	H 9	H 10	H 11	H 12	N 13
H	1													
H	2	-7.01												
F	3	-0.03	2.44											
F	4	2.40	0.01	0.02										
F	5	0.04	2.24	3.09	-0.07									
F	6	2.12	0.08	-0.10	2.01	-0.10								
H	7	0.04	1.90	0.33	0.04	-0.97	-0.17							
H	8	1.64	0.03	0.10	0.76	-0.18	-0.99	-0.32						
H	9	0.03	0.04	6.44	-0.04	6.04	-0.08	1.94	-0.02					
H	10	0.04	0.04	-0.03	6.17	-0.06	6.08	0.00	1.87	-0.05				
H	11	-0.04	1.74	-1.02	-0.08	1.04	-0.08	-0.43	0.00	2.00	-0.06			
H	12	1.66	0.19	-0.09	-1.13	-0.07	1.26	0.02	-0.43	-0.06	1.97	0.02		
N	13	-0.19	16.37	-3.59	0.00	-3.29	0.00	4.47	0.03	-0.09	0.00	4.17	-0.01	
N	14	16.26	-0.21	-0.05	-3.71	-0.03	-3.01	-0.02	4.55	0.00	-0.11	-0.04	4.13	0.00

S3 Additional discussion of experimental results

This section contains additional results and discussion that are not included in Section 4 of the main article.

S3.1 Polarisation-transfer field dependence

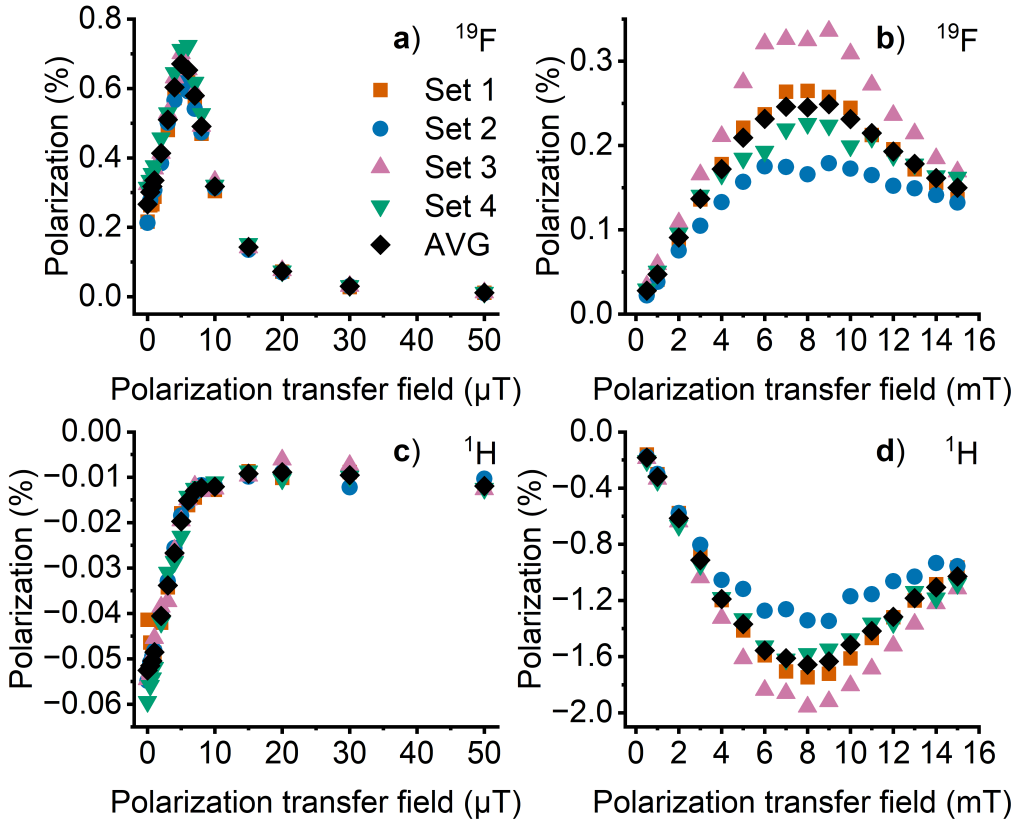

Figure S3: Effect of polarisation transfer field to the experimental polarisation levels of mFP from repeated sets of experiments. Polarisation of ^{19}F at (a) μT fields and (b) mT fields. Polarisation of ^{1}H at (c) μT fields and (d) mT fields.

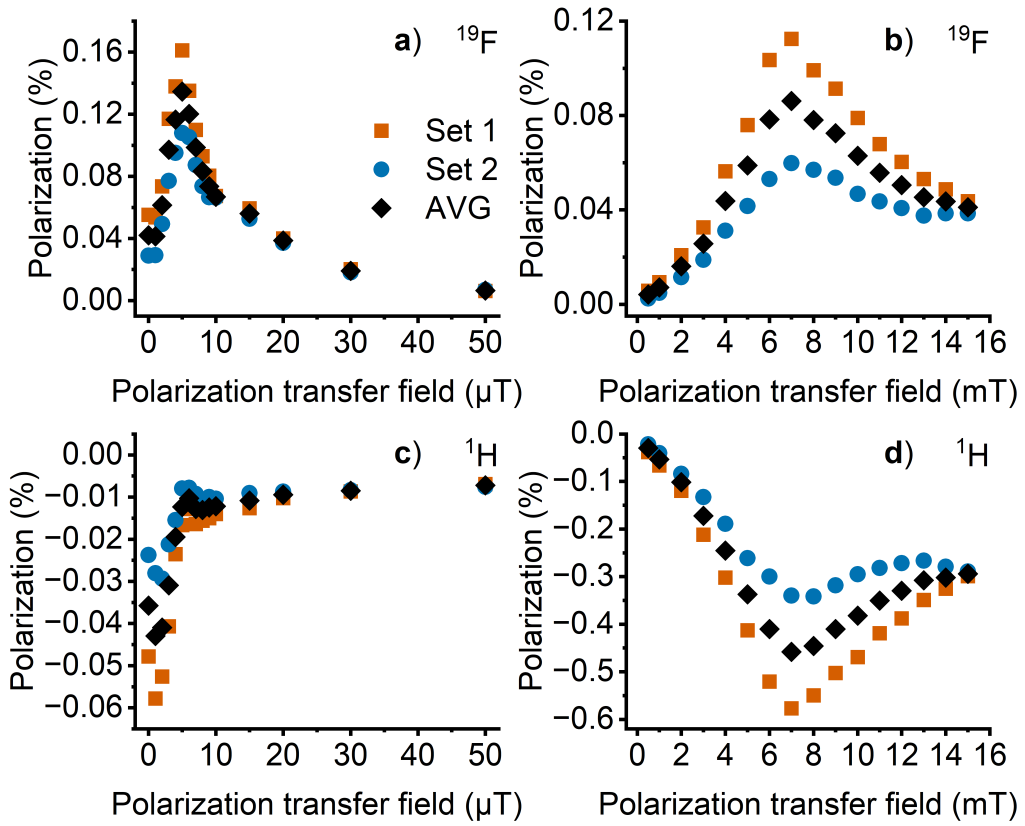

Figure S4: Effect of polarisation transfer field to the experimental polarisation levels of dFP from repeated sets of experiments. Polarisation of ^{19}F at (a) μT fields and (b) mT fields. Polarisation of ^{1}H at (c) μT fields and (d) mT fields.

The differences in the results are very systematic; each dataset is very consistent, but there are significant differences between the sets. The most likely explanation is the evaporation of the solvent and the substrate, since the SABRE efficiency is affected by the concentrations of the substrate and the catalyst.[21] A higher pH_2 pressure inside the NMR tube could be used to reduce evaporation. Due to the temperature dependence of SABRE,[22] changes in ambient temperature as well as chemical reactions, such as catalyst oligomerization,[23] could be additional causes of the systematic change in the observed level of polarisation as a function of time.

S3.1.1 Simplified model for coherent polarisation transfer

Polarisation transfer in SABRE is often attributed to coherent processes that take place under strong-coupling conditions, which occur at different magnetic-field strengths for different nuclei. This can be understood by considering the energy level anticrossings (LACs).[24,25] Considering an AA'B spin system composed of what used to be parahydrogen protons (AA') and the ^{19}F nucleus of mFP ligand (B), the two relevant initial states are $|S\alpha\rangle$ and $|S\beta\rangle$, where S denotes a singlet 2-spin state of the AA' spins and α/β denote the single-spin states of B. These states have the following LACs: $|S\alpha\rangle \longleftrightarrow |T_+\beta\rangle$ when $\nu_A - \nu_B = J_{AA'}$, and $|S\beta\rangle \longleftrightarrow |T_-\alpha\rangle$ when $\nu_A - \nu_B = -J_{AA'}$. The former LAC has no physical significance here, as it corresponds to a negative polarising field. The latter condition corresponds to $B_{\mathrm{LAC}} \approx 3.1$ μT. In this simple model, the estimated optimum field is slightly smaller than observed experimentally. When the system is kept at the LAC condition given by the latter equation, the initial state $|S\beta\rangle$ is no longer an eigenstate of the system, which causes the system to coherently oscillate between the states $|S\beta\rangle \longleftrightarrow |T_-\alpha\rangle$. As fresh parahydrogen is continuously being brought to the system, eventually the $|\beta\rangle$ ligand state will be depleted and the $|\alpha\rangle$ will be enriched. In other words, polarisation will be transferred from the AA' protons to the ^{19}F.

This three-spin model system is, however, an oversimplification of the experimental situation. Even with the full spin system, the LAC theory does not fully predict the dependence of the polarisation transfer field, as the spin system is subject to incoherent interactions in the forms of chemical exchange and relaxation, which may change the optimum magnetic field significantly.[26]

S3.2 Phase patterns of fluorine and proton spectra

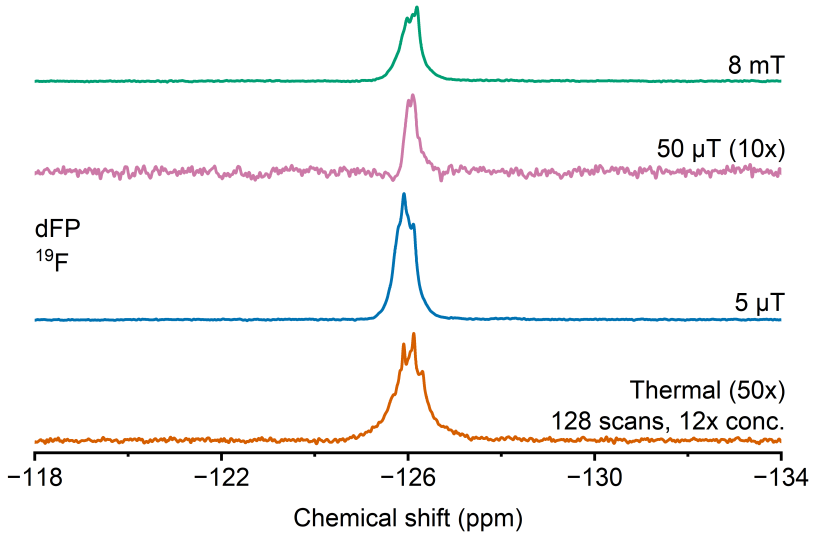

Figure S5: Comparison of ^{19}F spectra from SABRE-hyperpolarised dFP obtained at different magnetic fields. Also the thermal equilibrium spectrum is shown.

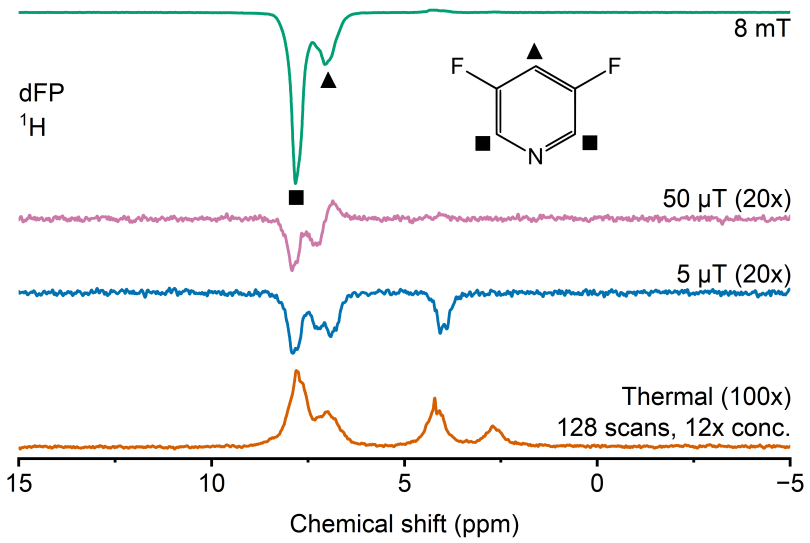

Figure S6: Comparison of ^{1}H spectra from SABRE-hyperpolarised dFP obtained at different magnetic fields. Also the thermal equilibrium spectrum is shown.

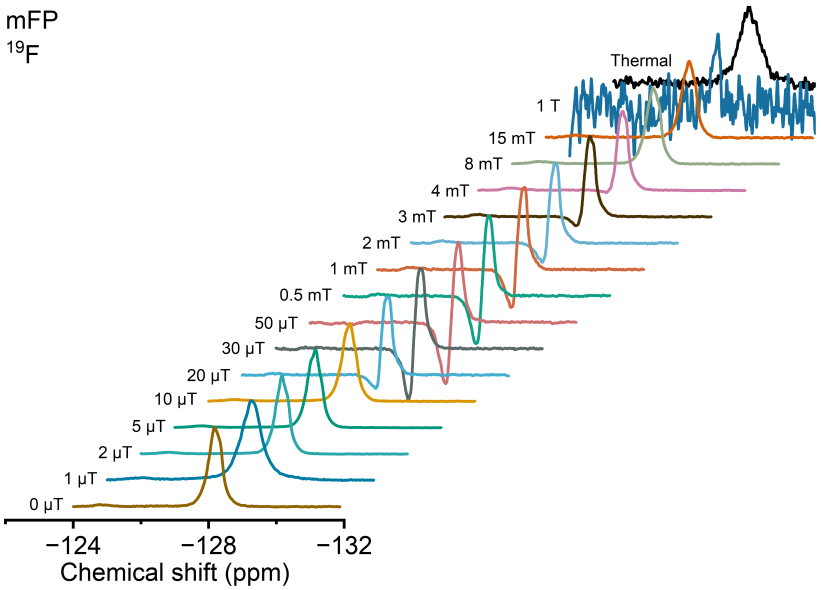

Figure S7: ^{19}F spectra from mFP at different polarisation transfer fields. The intensities have been normalized to increase readability.

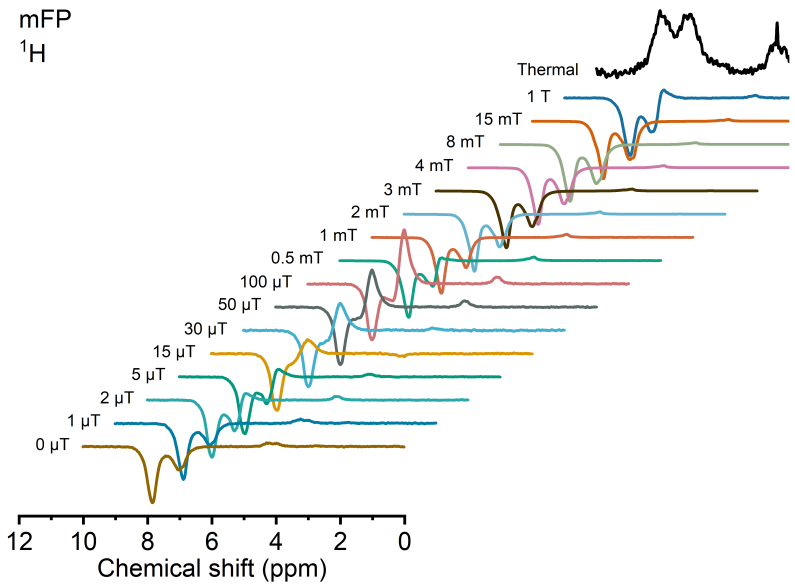

Figure S8: ^{1}H spectra from mFP at different polarisation transfer fields. The intensities have been normalized to increase readability.

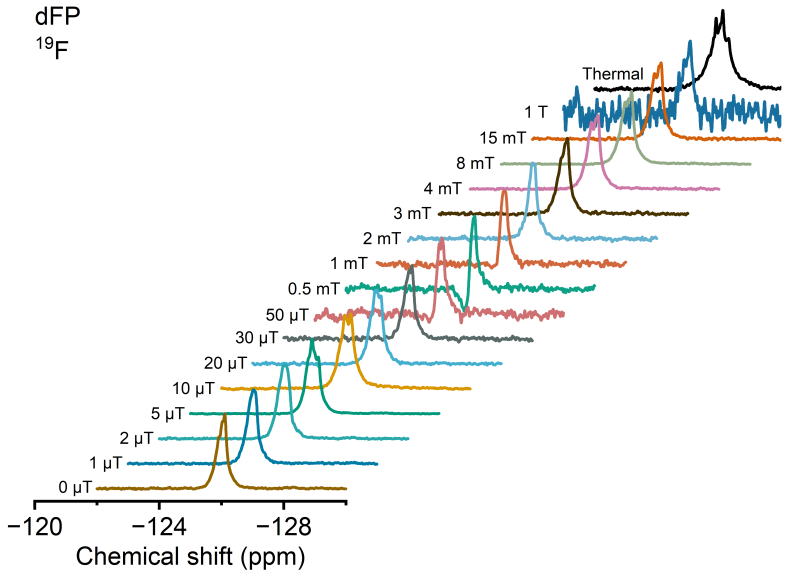

Figure S9: ^{19}F spectra from dFP at different polarisation transfer fields. The intensities have been normalized for increased readability.

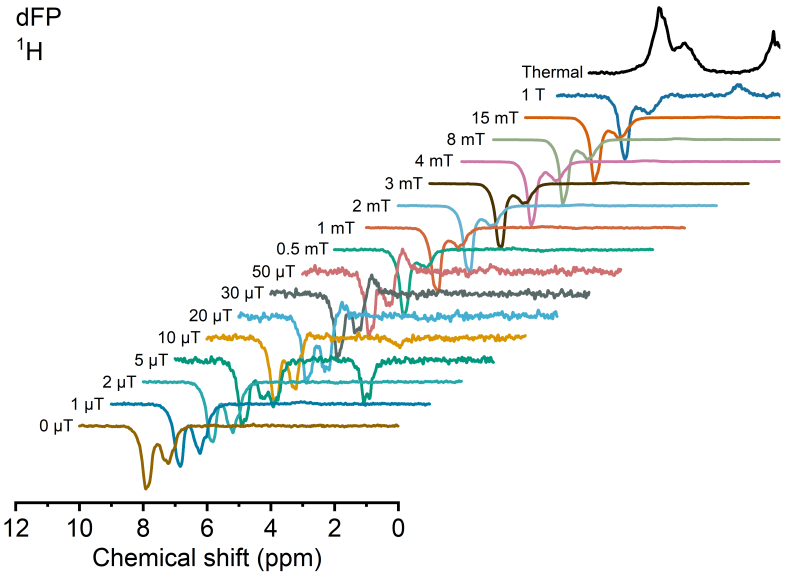

Figure S10: ^{1}H spectra from dFP at different polarisation transfer fields. The intensities have been normalized for increased readability.

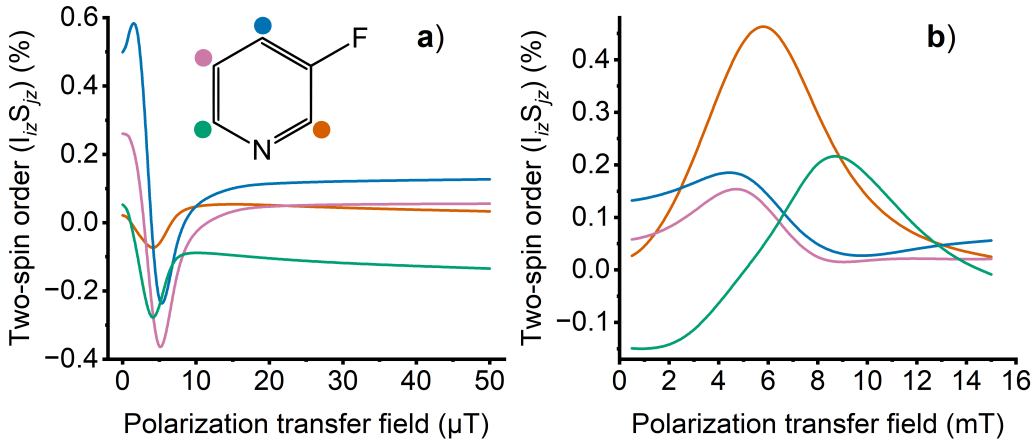

Figure S11: Simulated heteronuclear two-spin order coefficients at different polarisation transfer fields for mFP. In these simulations, the 14-spin model with coherent and incoherent interactions was used. (a) μT and (b) mT field strengths.

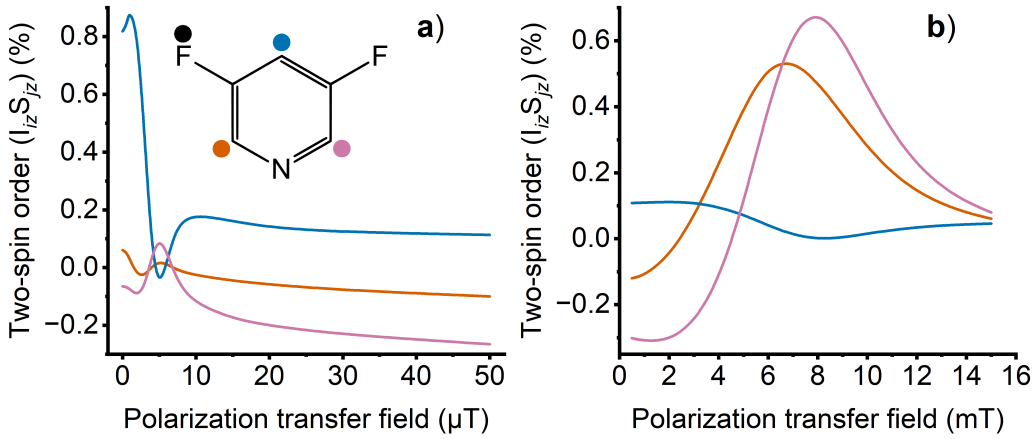

Figure S12: Simulated heteronuclear two-spin order coefficients at different polarisation transfer fields for dFP. In these simulations, the 14-spin model with coherent and incoherent interactions was used. (a) μT and (b) mT field strengths.

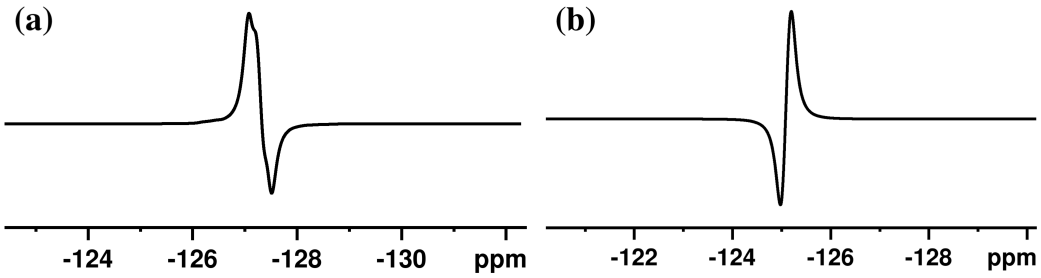

Figure S13: Theoretical ^{19}F spectra of (a) mFP and (b) dFP at 8 mT simulated with Bruker TopSpin NMRSim adopting the coefficients for S_z and I_zS_z from the simulations.

S3.3 Relaxation time analysis

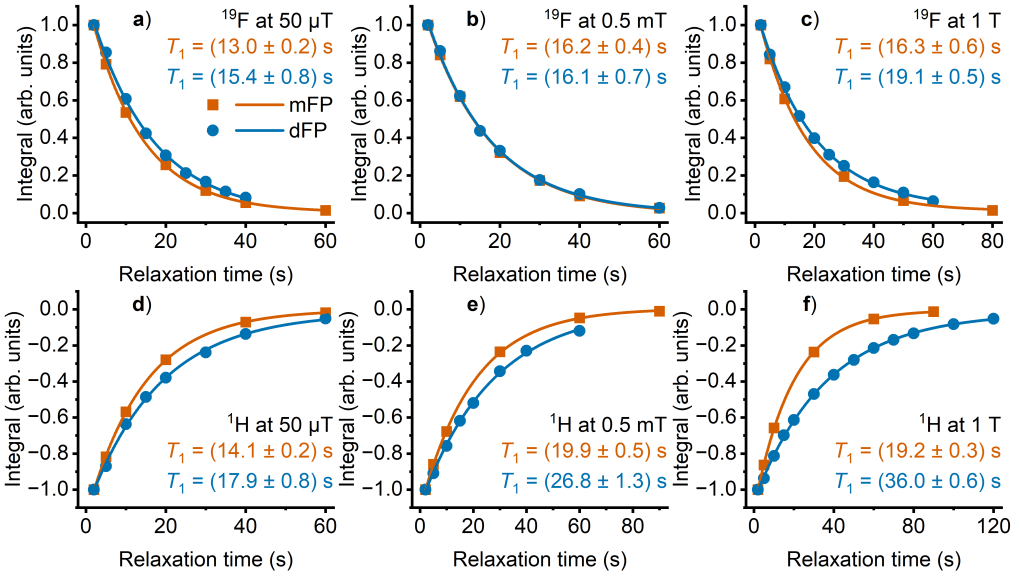

Figure S14: Relaxation time analysis of SABRE-hyperpolarised ^{19}F and ^{1}H nuclei at selected magnetic fields. ^{19}F at (a) 50 μT, (b) 0.5 mT and (c) 1 T. ^{1}H at (d) 50 μT, (e) 0.5 mT and (f) 1 T.

S3.4 Selective inversion-recovery experiments

The dissociation rate of mFP from the SABRE complex was measured at 298 K temperature by performing selective inversion-recovery experiments on a Bruker 600 MHz instrument. Substrate concentration was 90 mM and catalyst concentration was 3 mM. Higher concentrations than elsewhere in this project were used to ensure enough signal within a reasonable experiment time. The sample was prepared in a 5-mm valved medium-wall NMR tube. Two freeze-thaw cycles were performed to degas the sample. The catalyst activation was performed by pressurizing the NMR tube with hydrogen up to a 4-bar pressure (absolute) and shaking the sample vigorously for several minutes. To ensure proper activation, the hydrogen gas was replaced two times.

For a chemically exchanging system of n sites, the time dependence of

the magnetizations $M_n(t)$ follows the equation

$$\frac{\partial}{\partial t}\begin{bmatrix} M_1(\infty) - M_1(t) \\ \vdots \\ M_n(\infty) - M_n(t) \end{bmatrix} = -\boldsymbol{A}\begin{bmatrix} M_1(\infty) - M_1(t) \\ \vdots \\ M_n(\infty) - M_n(t) \end{bmatrix}, \tag{S2}$$

where $M_n(\infty)$ is the equilibrium magnetization of site n and $\boldsymbol{A}$ is the relaxation matrix

$$\boldsymbol{A} = \begin{bmatrix} \frac{1}{T_{11}} + \sum_{l\neq 1} k_{1l} & -k_{21} & -k_{31} & \dots & -k_{n1} \\ -k_{12} & \frac{1}{T_{12}} + \sum_{l\neq 2} k_{2l} & -k_{32} & \dots & -k_{n2} \\ \vdots & & & & \\ -k_{1n} & -k_{2n} & -k_{3n} & \dots & \frac{1}{T_{1n}} + \sum_{l\neq n} k_{nl} \end{bmatrix}, \tag{S3}$$

in which T_{1i} is the longitudinal relaxation time of site i, and k_{ij} is the exchange rate from site i to j.[27] The equation has the solution

$$\begin{bmatrix} M_1(t) \\ \vdots \\ M_n(t) \end{bmatrix} = \begin{bmatrix} M_1(\infty) \\ \vdots \\ M_n(\infty) \end{bmatrix} + \exp(-\boldsymbol{A}t)\begin{bmatrix} M_1(0) - M_1(\infty) \\ \vdots \\ M_n(0) - M_n(\infty) \end{bmatrix}. \tag{S4}$$

There are three possible chemical sites in the SABRE process: the solution, which we denote with S, the two equatorial positions in the complex, which we denote with C, and the axial position in the complex, which, based on our experimental data and previous SABRE experiments[28,29] does not exchange with the free solution (or exchanges extremely slowly). The system is therefore expressed as a two-site model, which obeys the equation

$$\begin{aligned} \begin{bmatrix} M_{\mathrm{C}}(t) \\ M_{\mathrm{S}}(t) \end{bmatrix} &= \begin{bmatrix} M_{\mathrm{C}}(\infty) \\ M_{\mathrm{S}}(\infty) \end{bmatrix} \\ &+ \exp\left(-\begin{bmatrix} \frac{1}{T_{1\mathrm{C}}} + k_{\mathrm{CS}} & -k_{\mathrm{SC}} \\ -k_{\mathrm{CS}} & \frac{1}{T_{1\mathrm{S}}} + k_{\mathrm{SC}} \end{bmatrix} t \right) \begin{bmatrix} M_{\mathrm{C}}(0) - M_{\mathrm{C}}(\infty) \\ M_{\mathrm{S}}(0) - M_{\mathrm{S}}(\infty) \end{bmatrix}. \end{aligned} \tag{S5}$$

In chemical equilibrium, the exchange rates k_{CS} and k_{SC} obey the following balance

$$k_{\mathrm{CS}} M_{\mathrm{C}}(\infty) = k_{\mathrm{SC}} M_{\mathrm{S}}(\infty). \tag{S6}$$

Using this and denoting $k_{\mathrm{CS}} = k_d$, we will arrive to the final equation

$$\begin{aligned}\begin{bmatrix} M_{\mathrm{C}}(t) \\ M_{\mathrm{S}}(t) \end{bmatrix} &= \begin{bmatrix} M_{\mathrm{C}}(\infty) \\ M_{\mathrm{S}}(\infty) \end{bmatrix} \\ &+ \exp\left(- \begin{bmatrix} \frac{1}{T_{1\mathrm{C}}} + k_d & -k_d \frac{M_{\mathrm{C}}(\infty)}{M_{\mathrm{S}}(\infty)} \\ -k_d & \frac{1}{T_{1\mathrm{S}}} + k_d \frac{M_{\mathrm{C}}(\infty)}{M_{\mathrm{S}}(\infty)} \end{bmatrix} t \right) \begin{bmatrix} M_{\mathrm{C}}(0) - M_{\mathrm{C}}(\infty) \\ M_{\mathrm{S}}(0) - M_{\mathrm{S}}(\infty) \end{bmatrix}.\end{aligned} \tag{S7}$$

The present experimental results and the fits to the data are shown in Fig. S15. The fit was obtained by performing a least-squares analysis to the experimental data in Python. The analysis could not fit the longitudinal relaxation time in the complex, so we ended up using the longitudinal relaxation time constant of the axial position, $T_{1\mathrm{C}} = 0.91 \pm 0.06$ s, which was determined using a regular inversion-recovery experiment. The parameters, their initial guesses, lower and upper bounds, the obtained values, and the standard deviations (SD), are shown in Table S12.

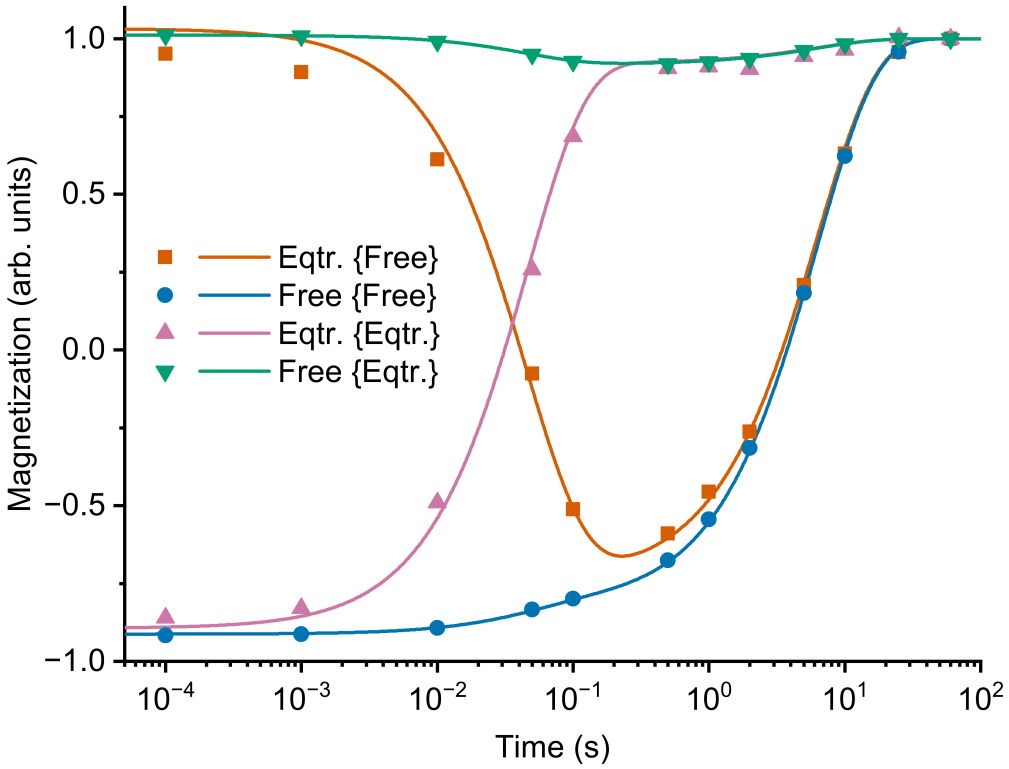

Figure S15: Results from fitting Eq. (S7). The magnetizations have been normalized for increased readability. The notation {Free} and {Eqtr.} refer to two different experiments where the magnetization of either the free or equatorial substrate is inverted.

Table S12: Parameters of the selective inversion-recovery experiment. The notations {Free} and {Eqtr.} refer to two different experiments where the magnetization of either the free or equatorial substrate is inverted.

Parameter	Initial guess	Lower bound	Upper bound	Result	SD
k_d (1/s)	10	0	100	19.6	1.0
T_{1S} (s)	10	0	100	9.0	1.3
T_{1C} (s)	-	-	-	0.91	0.06
$M_S(\infty)$	1	0	2	0.998	0.002
$M_C(\infty)$	0.05	0	2	0.0544	0.0011
$M_S(0)${Free}	-1	-2	0	-0.911	0.002
$M_C(0)${Free}	0.05	0	2	0.056	0.002
$M_S(0)${Eqtr.}	1	0	2	1.010	0.002
$M_C(0)${Eqtr.}	-0.05	-2	0	-0.049	0.002

Changing the ligand from mFP to dFP introduces more complexity to the exchange model, as there appears to be more than one active SABRE complex. This is seen in the NMR spectra acquired at 600 MHz, shown in Fig. S16. The ^{19}F spectrum shows several smaller signals arising from the dFP bound in different SABRE complexes. The formation of several complexes is also demonstrated in the ^{1}H spectrum of the hydride region, where multiple hydride signals are displayed. Selective inversion-recovery experiments could not be used to determine the dissociation rate of dFP at 298 K due to the small signal of the complex-bound dFP, as well as due to the short lifetime of the complexes.

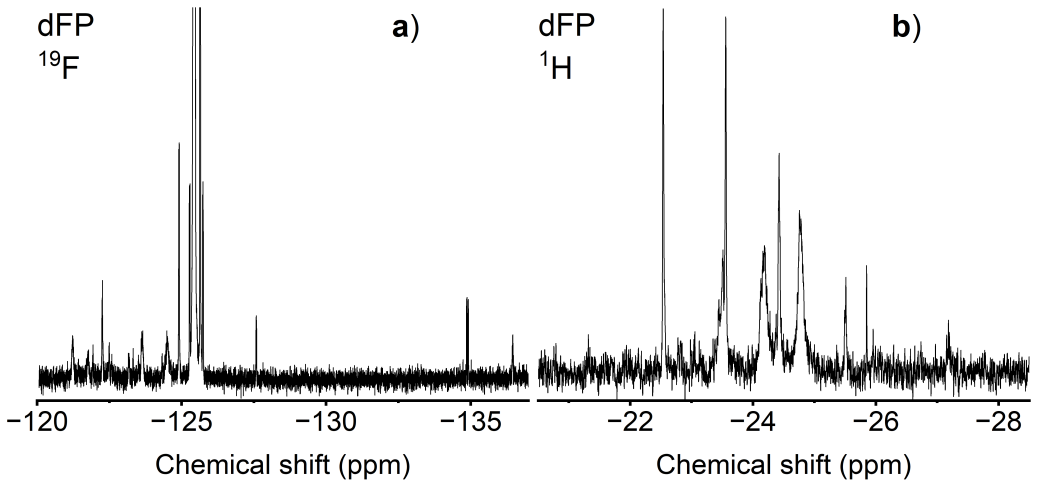

Figure S16: 16-scan NMR spectra of dFP SABRE sample acquired at 600 MHz. a) ^{19}F spectrum of the free and complex-bound dFP. b) ^{1}H spectrum of the hydride region.

S4 Simulation results

In the comparison of simulated and experimental polarisation of ligand nuclei in Figs. 3, S17-S20, the results from the spin dynamics simulations have been scaled to fit the scale of the experimental results. The scaling factors are shown in Table S13. Tabulated simulation results can be found as an attachment "tabulated_values.zip". To go from the tabulated magnetization values to spin polarisation percentages shown in the figures, we divide the magnetization $\langle \hat{I}_z \rangle$ by the spin quantum number I, and multiply by both 100% and the scaling factor:

$$P(\%) = \frac{\langle \hat{I}_z \rangle}{I} \cdot 100\% \cdot \text{scaling factor.} \tag{S8}$$

Table S13: Scaling factors used in all of the corresponding simulations.

Substrate	Nucleus	Field range	Scaling factor
mFP	^{19}F	μT	0.47
		mT	63
	^{1}H	μT	3.4
		mT	1.5
dFP	^{19}F	μT	0.085
		mT	23
	^{1}H	μT	0.30
		mT	0.27

S4.1 Role and path of incoherent interactions in mFP

Figure S17 shows the polarisation of ^{19}F and ^{1}H in mFP as a function of magnetic field for the 14-spin model. An overall finding is that the best simulations, in which incoherent interactions are included, always reproduce the experimental signs of the polarisation for both ^{1}H (negative) and ^{19}F (positive) in the two magnetic-field regimes, mT and μT ranges. The profiles of the magnetization as functions of the field strength have qualitatively mostly the correct shape, although the simulated, small ^{1}H polarisation in the μT regime does switch over to small positive polarisation from about 10 μT onwards, in contrast to the experimental findings. In the other three cases, the location of the polarisation maxima and their general shape are well-reproduced.

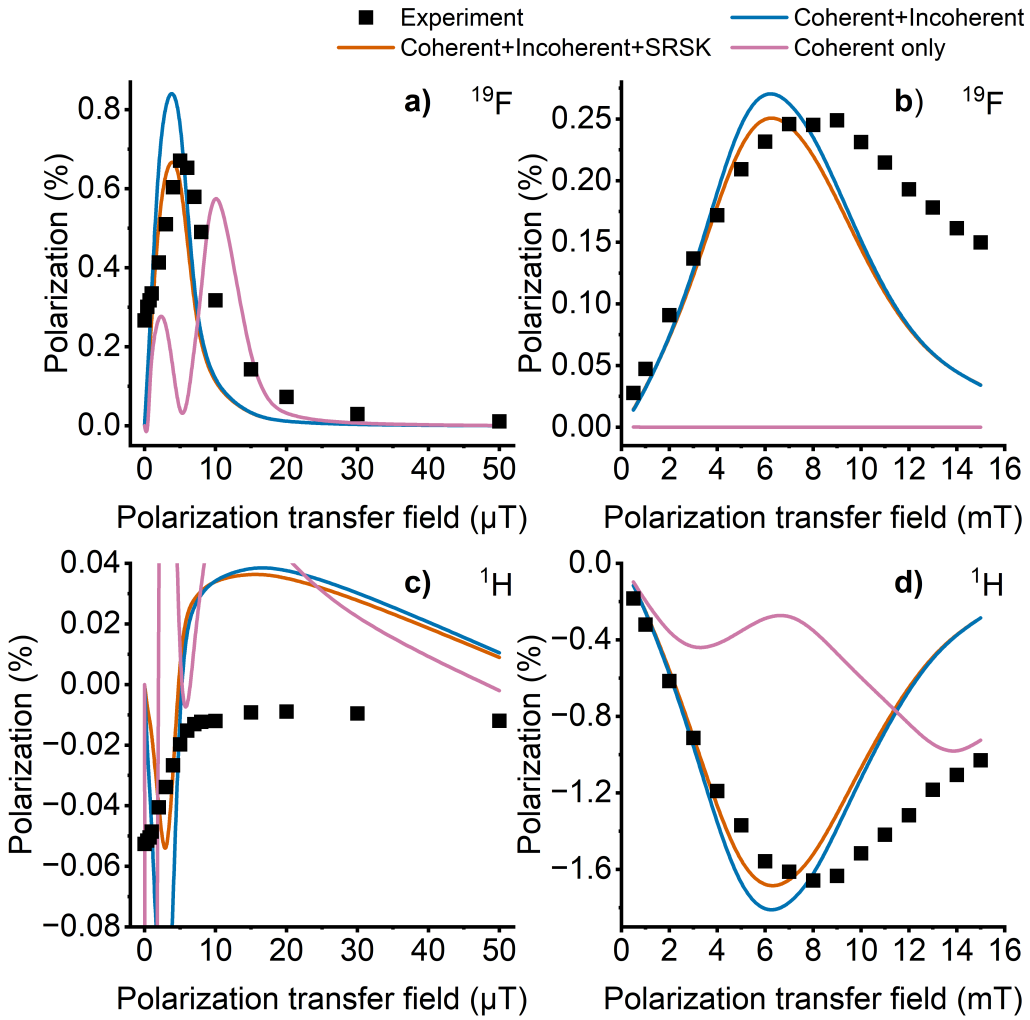

Figure S17: Comparison between the polarisation levels of mFP calculated with different NMR interactions using the 14-spin model. The basis set is restricted to include maximally 4-spin order. The simulations are scaled to fit the experimental results. For the scaling factors, refer to Table S13. ^{19}F at (a) μT fields and (b) mT fields. ^{1}H at (c) μT fields and (d) mT fields.

It is noteworthy that the simulations performed without including incoherent interactions fail in all cases to reproduce the qualitative characteristics of the polarisation-field profiles. Comparing simulations with and without relaxation, it can be seen that ^{19}F in μT fields and ^{1}H in both μT and mT

fields do become polarised both when relaxation is included and when it is not. Thus, polarisation transfer to these ligand spins from the hydride, at these magnetic fields, can be assumed to be in large part due to coherent mechanisms operating via level anticrossings. The most notable aspect of the results from the purely coherent simulations is that none of the employed models (see below in Fig. S19) lead to any significant polarisation of ^{19}F at mT-fields. Thus, it can be concluded that cross-relaxation is necessary to transfer polarisation to ^{19}F in mT-fields. The big qualitative difference in the shape of the curves between purely coherent simulations and simulations that also include incoherent mechanisms is explained in the discussion of Fig. S18 and S19 below. Briefly, comparing simulations with and without ^{14}N shows that incorporating these nuclei in the simulations when incoherent interactions are omitted, results in a build-up of ^{14}N polarisation which would not take place with incoherent interactions enabled — due to the fast relaxation rate of ^{14}N. Thus, results from coherent simulations with ^{14}N are qualitatively very different. Comparing the results including relaxation, but with and without SRSK, it can be seen that SRSK makes a noticeable quantitative difference (a slight decrease of both ^{19}F and ^{1}H polarisation at both field regimes), but there is no qualitative overall change.

Test simulations including incoherent mechanisms but from which all fluoropyridine ^{1}H centres were excluded, *i.e.*, a 6-spin system including ^{14}N and ^{19}F from both fluoropyridine ligands, results in the ^{19}F centres acquiring $\sim 9 \times 10^{-3}\hbar$ polarisation at 5 μT and $\sim 5 \times 10^{-8}\hbar$ at 8 mT. The corresponding, more complete simulations that also included all the ^{1}H centres of the fluoropyridines, *i.e.*, a total of 14 spins, gave a rather similar $\sim 7 \times 10^{-3}\hbar$ polarisation at 5 μT and the vastly larger $\sim 2 \times 10^{-5}\hbar$ at 8 mT. Thus, the polarisation of ^{19}F at 5 μT retains its magnitude even if all the ligand ^{1}H are removed. In contrast, the polarisation at 8 mT decreases by more than two orders of magnitude, upon removal of the ligand protons. This indicates that the coherent mechanism responsible for most of the polarisation transfer from the hydrides to the ^{19}F at μT fields is largely provided by a direct connection between the spins. On the other hand, it can be seen that the polarisation transfer between the hydride protons and ^{19}F centres at mT fields proceeds via the fluoropyridine protons. In this process, the ^{1}H centres of the ligands are polarised, mostly through coherent mechanisms, and subsequently the polarisation is transferred from the ^{1}H nuclei to ^{19}F through cross-relaxation.

Simulations including just one ^{1}H centre per fluoropyridine, the one be-

tween the ^{14}N and the ^{19}F (protons number 5 and 6 in Fig. S2), again lead to ^{19}F spin polarisations of $\sim 9 \times 10^{-3}\hbar$ at 5 μT and $\sim 2 \times 10^{-5}\hbar$ at 8 mT, which is comparable to the results obtained with all the pyridine ^{1}H centres retained, indicating that this proton (in position 2 of the ligand) is the most important one for the polarisation transfer to ^{19}F, thus strengthening this model of explanation. It makes physical and chemical sense for this particular ^{1}H centre to be the most important one, since it is the only proton that both has a strong (> 1 Hz) J-coupling to one of the hydride protons and is spatially close to the ^{19}F centre of the same ligand.

S4.2 Effect of the choice of rotational correlation time

14-spin simulations that included the incoherent mechanisms but which were carried out with altered rotational correlation times of 10 ps and 100 ps rather than the value of 30 ps chosen based on the inversion-recovery experiments, were run for comparison. For ^{19}F, the change of the rotational correlation time led to a relative change of the polarisation level by -42% and $+34\%$ for $\tau_c = 10$ and 100 ps, respectively, at 5 μT and, correspondingly, -73% and $+240\%$ at 8 mT, compared to the results obtained with the rotational correlation time of 30 ps. For ^{1}H, the changes of the polarisation level equal -19% and $+5\%$ at 8 mT. At μT fields, the ^{1}H polarisation has a less well-behaved curve shape, and comparison becomes less straightforward. The assumption of isotropic rotational diffusion as the dynamical model for the relaxation is a significant approximation. There does not necessarily exist a perfect value of the rotational correlation time that would give the universally "best" simulation results. As can be seen from this test, a change of the correlation time by a factor of ~ 3 can cause a large change in the amplitude of the polarisation curves. For this reason, the scaling factors (Table S13), necessary for a qualitative comparison with experimental field profiles of polarisation, will be completely dependent on the choice of rotational correlation time.

S4.3 Model size and reduction of the operator basis set

Figures S18 and S19 show the polarisation of ^{19}F and ^{1}H in mFP as a function of magnetic field, for models with different number of spins. In Fig. S18, relaxation (incoherent interactions) is included, whereas in Fig. S19, only the coherent mechanisms are included in the dynamics.

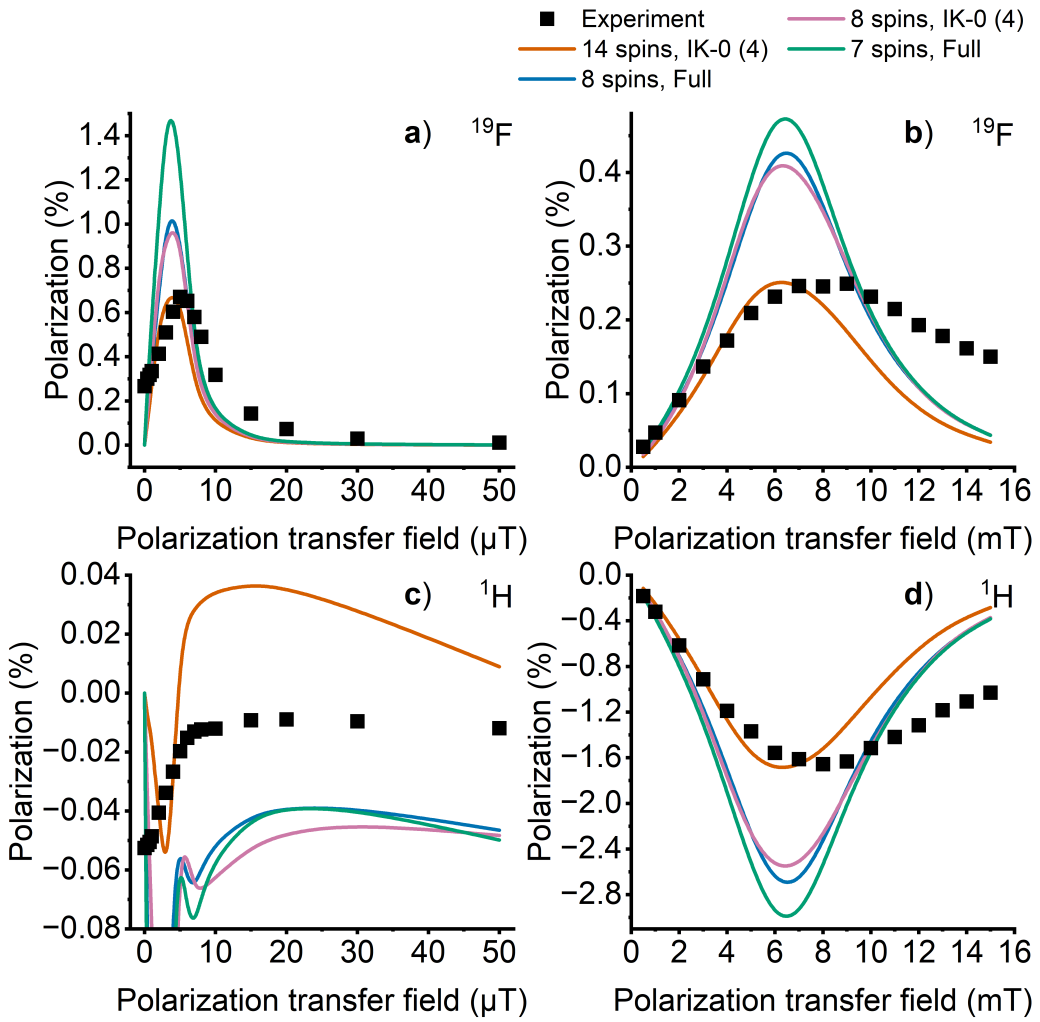

Figure S18: Comparison between the polarisation levels of mFP calculated with both coherent and incoherent interactions, using different spin systems and basis-set approximations. The legend describes the size of the spin system and whether all possible spin orders (Full) or, at maximum, 4-spin order [(IK-0 (4)] is used in the basis set. The simulations are scaled to fit the experimental results. For the scaling factors, refer to Table S13. ^{19}F at (a) μT fields and (b) mT fields. ^{1}H at (c) μT fields and (d) mT fields.

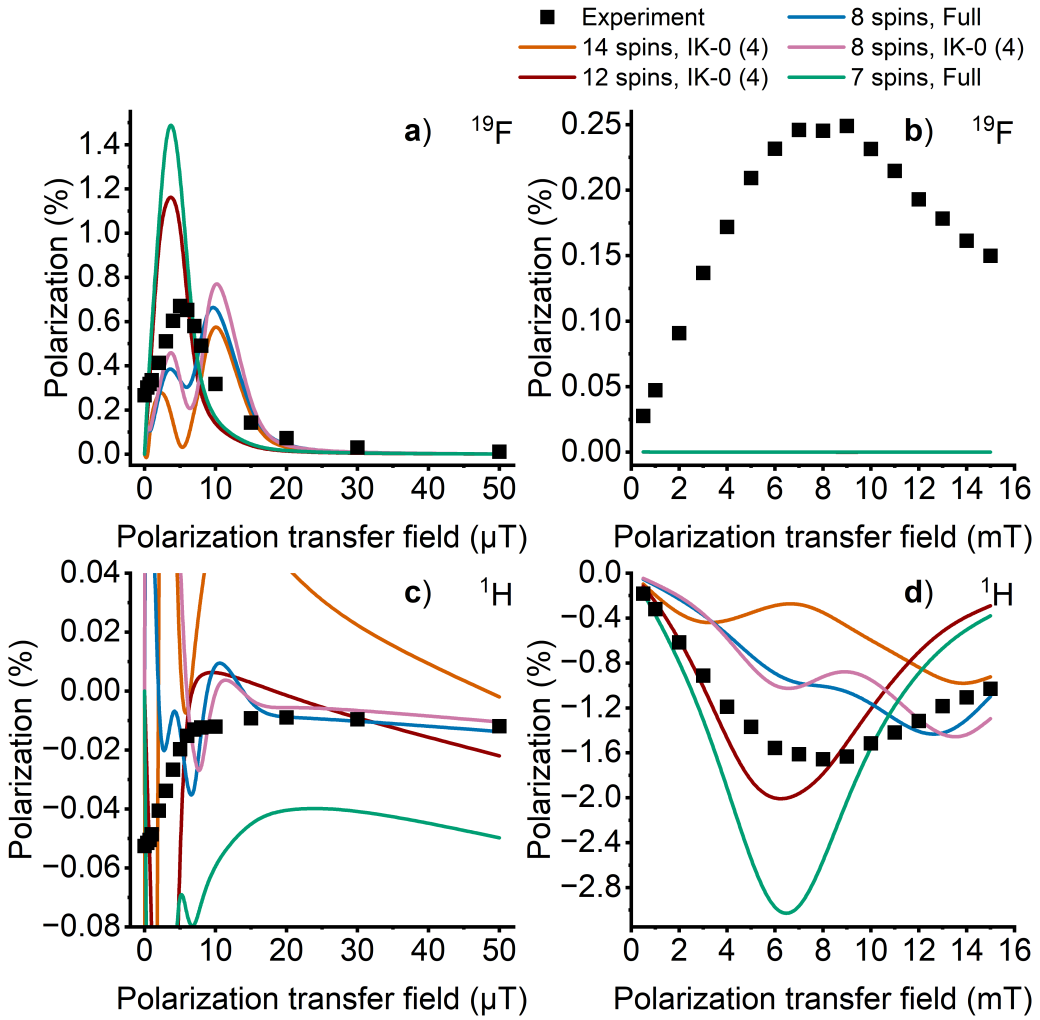

Figure S19: Comparison between the polarisation levels of mFP calculated with only the coherent interactions, using different spin systems and basis-set approximations. The legend describes the size of the spin system and whether all possible spin orders (Full) or, at maximum, 4-spin order [IK-0 (4)] was used in the basis set. The simulations are scaled to fit the experimental results. For the scaling factors, refer to Table S13. ^{19}F at (a) μT fields and (b) mT fields. ^{1}H at (c) μT fields and (d) mT fields.

When comparing the 8-spin simulations with the simplified IK-0 (4) approximation and the full spin operator basis set, it can be seen that the results

remain semiquantitatively similar in the approximate calculations. Only a small decrease of the ^{19}F polarisation at both μT and mT field ranges, as well as the same in the ^{1}H polarisation at the mT range take place as a result of simplifying the basis set. Considering all the other model approximations adopted in this work, the small differences in the results between the basis sets are not important.

On the other hand, by comparing simulations with both or just one equatorial pyridine ligand, it can be seen that having just one ligand leads to an increased magnitude of polarisation of ^{19}F at both μT- and mT-fields (except for purely coherent simulations), as well as for ^{1}H at mT-fields. The degree of spin order originating from the pH_2 is, in the two-ligand case, shared between more nuclei, resulting in generally reduced overall polarisation levels of the ligand nuclei in that case. However, one has to bear in mind that, in the cross relaxation-mediated mechanism of polarising the ^{19}F nuclei, the presence of ^{1}H nucleus or nuclei in the ligand is crucial, as the proton(s) become first polarised primarily coherently, and only then incoherently relay their polarisation to fluorine. Hence, it would be too simple to state that the smaller spin system, the better polarisation levels would be achieved.

S4.4 Role of quadrupolar ^{14}N

Looking at the simulations with relaxation, Fig. S18, for the single pyridine ligand simulations, excluding the ^{14}N centre from the spin system leads to a higher magnitude of polarisation. This increase takes place both for ^{19}F and ^{1}H centres at all field strengths. The quadrupolar ^{14}N acts as a spin-polarisation sink and, consequently, removing it means that overall less polarisation is removed by relaxation.

For the purely coherent simulations, Fig. S19, a major difference can be seen between the simulations that include ^{14}N (the 14- and 8-spin models) and those that do not include the ^{14}N centre (12- and 7-spin models). Noticeably, the results from the coherent simulations that do not include ^{14}N are, in fact, more similar to the results obtained for the full 14-spin system including the incoherent interactions, than the results from coherent-only simulations that do include ^{14}N. This can again be understood through the fact that, in the incoherent simulations, ^{14}N almost exclusively acts as a polarisation sink and does not acquire any noticeable spin polarisation of its own. The coherent dynamics of ^{14}N are thus completely overshadowed by the incoherent interactions, effectively decoupling this centre from the rest of the spin

system. In the coherent-only models, ^{14}N no longer provides a polarisation sink and is able to gain spin polarisation and have coherent spin dynamics of its own. Hence, a coherent dynamic model should preferentially omit the ^{14}N centre: The change when going from an incoherent simulation including ^{14}N to a purely coherent simulation including ^{14}N can be considered, apart from the smaller change related to the direct dipole-dipole interaction, as removing a polarisation sink and adding a spin to be polarised. In contrast, the change when going from an incoherent simulation including ^{14}N to a purely coherent simulation not including ^{14}N, can be considered as removing the polarisation sink without altering the active number of spins.

S4.5 Different models for dFP

Figure S20 shows the polarisation of ^{19}F and ^{1}H in dFP as a function of the magnetic field. The simulated polarisation profile for dFP is qualitatively similar to the one for mFP. The comparisons between simulations with and without relaxation, and 14-spin compared to 12-spin, support the same qualitative arguments as made in the mFP case.

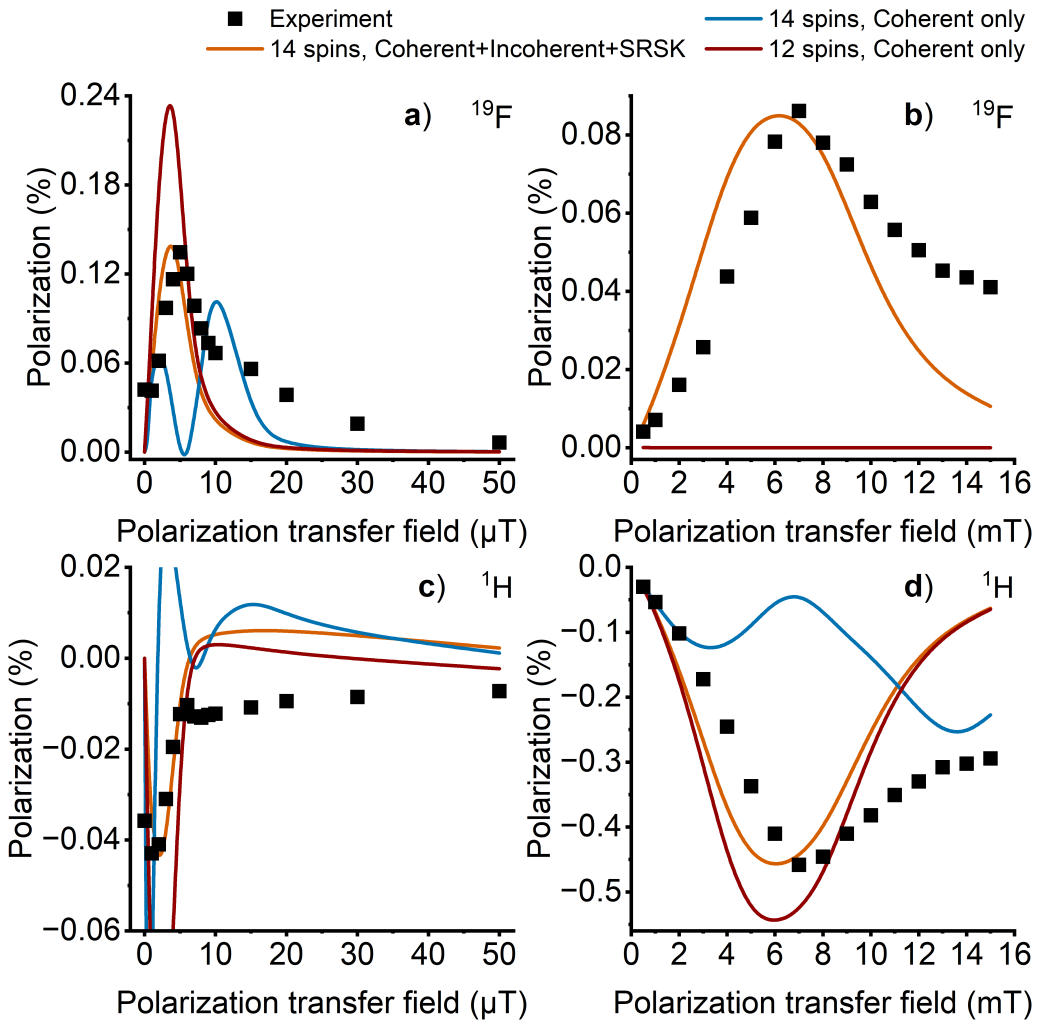

Figure S20: Comparison between the polarisation levels of dFP calculated with different NMR interactions and spin systems. The legend describes the size of the spin system and the interactions that are considered. The basis set was restricted to include, at maximum, 4-spin order. The simulations are scaled to fit the experimental results. For the scaling factors, refer to Table S13. ^{19}F at (a) μT fields and (b) mT fields. ^{1}H at (c) μT fields and (d) mT fields.

S4.6 Discussion of possible model deficiencies

The present simulations do not quantitatively reproduce the experimental magnetization transfer behaviour as a function of the magnetic-field strength. Instead, there is a need for multiplicative scaling factors (Table S13) to render the comparison of experiment and computational results feasible. The reason for this is in the approximations of the computational model, which first and foremost include the fact that we do not presently include the exchange of the hydride protons, but only that of the ligands. Preliminary simulations with an improved model including both the ligand and hydride exchange in related SABRE complexes indicate that substantially improved, semi-quantitative agreement with experiment can then be obtained. These results will be published separately.

An issue of its own is the inherent model assumption that only the above-mentioned two exchange reactions take place, which omits the possibly relevant reaction intermediates.[9] As discussed in the main text, there are indications that, especially in the case of dFP, this picture is too simple.

One aspect of the different scaling factors in Table S13 is that much larger values are required for the ^{19}F nucleus in the mT field range, than for both ^{1}H in the μT and mT realms, as well as ^{19}F in the μT range. This can be understood qualitatively on the basis of the fact that a two-step process, primarily coherent transfer to ligand ^{1}H and subsequent incoherent polarisation of the ^{19}F, is involved for the latter nuclei, at the higher field strengths. This suggests the possibility that both of these processes would need a roughly similar empirical scaling factor, to reach the level of experimental results, explaining the much larger scaling factors in this case.

The second major simplification resides in the adopted motional model, which is isotropic rotational diffusion of the rigid SABRE complex. This model neglects internal low-frequency motions, such as wobbling of the equatorial ligands, which could incur dissipation of the nuclear spin dynamics and, hence, affect the polarisation-field profile, as well as the build-up and relaxation dynamics. The single rotational correlation time value adopted for the entire complex cannot be entirely uniquely chosen, and the choice affects the quantitative simulation results significantly. Going beyond this simple model would require consideration of the conformational dynamics of the complexes, which provides an interesting topic for further work.

Another shortcoming regarding the current treatment of dissipation is the adopted Redfield theory framework (2^{nd}-order perturbation theory), supple-

mented with an empirical account of SRSK effects. While the Redfield theory allows the description of cross relaxation-mediated hyperpolarization pathways, it does not provide the full description of spin dynamics when far from the equilibrium state.[30] In particular, due to the assumption of equal transition probabilities, the Redfield relaxation superoperator, even when thermalized with the Levitt-di Bari method,[7] does not capture the non-adiabatic contributions to the coherence decay rates,[30] which possibly results in inconsistent relaxation effects, especially in the multi-step polarization transfer pathways. However, this is most likely a minor issue in the present work, as the nuclear spins are relatively strongly coupled, leading to spin dynamics being dominated by the coherent interactions. A more accurate description of the relaxation would be achieved using the Lindblad formalism, making it a valuable topic for further research.

The employed quantum-chemical model, DFT calculations for the rigid complex *in vacuo*, limits the attainable precision of the calculated spin Hamiltonian parameters. As the most critical single-bond couplings to the ^{19}F centres are not involved in the present, non-^{13}C enriched substances, the use of DFT instead of the computationally much more demanding *ab initio* wave function theory approaches most likely does not present a major source of error here. Combined with the incorporation of conformational flexibility, involving a solvent in the parametrisation of the spin Hamiltonian represents an obvious avenue for model improvement.

References

[1] I. Kuprov, N. Wagner-Rundell and P. Hore, *J. Magn. Reson.*, 2007, **189**, 241–250.

[2] A. Karabanov, I. Kuprov, G. T. P. Charnock, A. van der Drift, L. J. Edwards and W. Köckenberger, *J. Chem. Phys.*, 2011, **135**, 084106.

[3] A. G. Redfield, *IBM J. Res. Dev.*, 1957, **1**, 19–31.

[4] R. K. Wangsness and F. Bloch, *Phys. Rev.*, 1953, **89**, 728–739.

[5] I. Kuprov, *J. Magn. Reson.*, 2011, **209**, 31–38.

[6] A. Abragam, *The Principles of Nuclear Magnetism*, Clarendon Press, Oxford, 1961.

[7] M. H. Levitt and L. Di Bari, *Phys. Rev. Lett.*, 1992, **69**, 3124–3127.

[8] A. Browning, K. Macculloch, P. TomHon, I. Mandzhieva, E. Y. Chekmenev, B. M. Goodson, S. Lehmkuhl and T. Theis, *Phys. Chem. Chem. Phys.*, 2023, **25**, 16446–16458.

[9] K. Lin, P. TomHon, S. Lehmkuhl, R. Laasner, T. Theis and V. Blum, *ChemPhysChem*, 2021, **22**, 1947–1957.

[10] J. R. Lindale, S. L. Eriksson, C. P. N. Tanner and W. S. Warren, *Sci. Adv.*, 2020, **6**, eabb6874.

[11] TURBOMOLE V7.2 2017, a development of University of Karlsruhe and Forschungszentrum Karlsruhe GmbH, 1989-2007, TURBOMOLE GmbH, since 2007, available from http://www.turbomole.com.

[12] C. Adamo and V. Barone, *J. Chem. Phys.*, 1999, **110**, 6158–6170.

[13] S. Grimme, J. Antony, S. Ehrlich and H. Krieg, *J. Chem. Phys.*, 2010, **132**, 154104.

[14] S. Grimme, S. Ehrlich and L. Goerigk, *J. Comput. Chem.*, 2011, **32**, 1456–1465.

[15] D. Figgen, K. A. Peterson, M. Dolg and H. Stoll, *J. Chem. Phys.*, 2009, **130**, 164108.

[16] D. Andrae, U. Häußermann, M. Dolg, H. Stoll and H. Preuß, *Theor. Chim. Acta*, 1990, **77**, 123–141.

[17] F. Weigend and R. Ahlrichs, *Phys. Chem. Chem. Phys.*, 2005, **7**, 3297–3305.

[18] J. Vícha, S. Komorovsky, M. Repisky, R. Marek and M. Straka, *J. Chem. Theory Comput.*, 2018, **14**, 3025–3039.

[19] J. Vícha, J. Novotný, S. Komorovsky, M. Straka, M. Kaupp and R. Marek, *Chem. Rev.*, 2020, **120**, 7065–7103.

[20] D. A. Matthews, L. Cheng, M. E. Harding, F. Lipparini, S. Stopkowicz, T. C. Jagau, P. G. Szalay, J. Gauss and J. F. Stanton, *J. Chem. Phys.*, 2020, **152**, 214108.

[21] M. L. Truong, T. Theis, A. M. Coffey, R. V. Shchepin, K. W. Waddell, F. Shi, B. M. Goodson, W. S. Warren and E. Y. Chekmenev, *J. Phys. Chem. C*, 2015, **119**, 8786–8797.

[22] H. Zeng, J. Xu, J. Gillen, M. T. McMahon, D. Artemov, J.-M. Tyburn, J. A. Lohman, R. E. Mewis, K. D. Atkinson, G. G. Green, S. B. Duckett and P. C. van Zijl, *J. Magn. Reson.*, 2013, **237**, 73–78.

[23] M. L. Truong, F. Shi, P. He, B. Yuan, K. N. Plunkett, A. M. Coffey, R. V. Shchepin, D. A. Barskiy, K. V. Kovtunov, I. V. Koptyug, K. W. Waddell, B. M. Goodson and E. Y. Chekmenev, *J. Phys. Chem. B*, 2014, **118**, 13882–13889.

[24] A. N. Pravdivtsev, A. V. Yurkovskaya, H.-M. Vieth, K. L. Ivanov and R. Kaptein, *ChemPhysChem*, 2013, **14**, 3327–3331.

[25] A. N. Pravdivtsev, K. L. Ivanov, A. V. Yurkovskaya, P. A. Petrov, H.-H. Limbach, R. Kaptein and H.-M. Vieth, *J. Magn. Reson.*, 2015, **261**, 73–82.

[26] S. L. Eriksson, J. R. Lindale, X. Li and W. S. Warren, *Sci. Adv.*, 2022, **8**, eabl3708.

[27] A. Bain and J. Cramer, *J. Magn. Reson., Series A*, 1993, **103**, 217–222.

[28] L. S. Lloyd, A. Asghar, M. J. Burns, A. Charlton, S. Coombes, M. J. Cowley, G. J. Dear, S. B. Duckett, G. R. Genov, G. G. R. Green, L. A. R. Highton, A. J. J. Hooper, M. Khan, I. G. Khazal, R. J. Lewis, R. E. Mewis, A. D. Roberts and A. J. Ruddlesden, *Catal. Sci. Technol.*, 2014, **4**, 3544–3554.

[29] R. V. Shchepin, M. L. Truong, T. Theis, A. M. Coffey, F. Shi, K. W. Waddell, W. S. Warren, B. M. Goodson and E. Y. Chekmenev, *J. Phys. Chem. Lett.*, 2015, **6**, 1961–1967.

[30] C. Bengs and M. H. Levitt, *J. Magn. Reson.*, 2020, **310**, 106645.